

Supporting Information

Dixon et al. 10.1073/pnas.1412299111

GPS Data Analysis

GPS data analysis and error estimation follow ref. 1. Briefly, GPS observations are used to estimate 24-h average positions, using the GIPSY/OASIS (GPS Inferred Positioning System/Orbit Analysis Software) software in the precise point positioning mode (2). Observations with less than 4 h of observations are deleted. Fiducial-free orbit data from the Jet Propulsion Lab are used to produce fiducial-free station coordinates. Daily site coordinates are then transformed to the ITRF (International Terrestrial Reference Frame) 2008 reference frame (3) using daily transformation parameters also provided by the Jet Propulsion Lab. The Wide Lane Phase Bias (4) solutions are adopted for calculating cycle ambiguities in the GPS observations. This algorithm is able to resolve ambiguities with single station observations, which improves the GPS time series repeatability by ~30% in the east direction. The postfit WRMS (weighted root mean square scatter) for a linear plus seasonal time series model fit to the raw position data are 3 mm, 3 mm, and 8 mm for the north, east, and vertical components, respectively. Regional filtering (5) and modeling the SSEs (1) reduces postfit WRMS to 2 mm, 2 mm, and 6 mm for the three position components. The positionogram method (1) is used to identify the onset of the SSEs in the GPS time series. Velocity uncertainties from analysis of the GPS postfit residuals using a white plus colored noise model are 0.1 mm/y for the horizontal component estimates and 0.5 mm/y for the vertical component.

All velocities from the GPS time series are initially in the ITRF 2008 reference frame. A local rotation pole is used to transform these to the stable Caribbean Plate reference frame (6) following procedures outlined in our previous studies (1, 7–9). A model for the GPS time series is then developed that accounts for inter-SSE velocity, seasonal variation, and SSE timing, duration, and displacement (1).

Inversions for Slip at Depth

We use the TDefnode software package (10) to invert our geodetic measurements. TDefnode simultaneously estimates long-term block rotation, interseismic or inter-SSE locking on fault surfaces, and transient sources such as SSEs. The Earth's crust is defined by a series of plates or blocks separated by active faults. Block motions are specified by rotation about Euler poles, and strain accumulation along block boundaries is specified by the backslip model (11). Block boundaries are faults that are represented by 3D irregular grids of nodes defined by latitude, longitude, and depth. For this work, the fore-arc block (8, 9) is defined separately from the Cocos and Caribbean plates. The fore-arc block is bounded by a right-lateral strike-slip fault to the northeast and the dipping subduction interface to the southwest. The strike slip fault separating the fore-arc block and Caribbean plate is assumed to be vertical and to run through the active volcanic chain. The thrust fault separating the fore-arc block from the Cocos plate dips at a value specified by the slab model (12). Additional constraints include Centroid Moment Tensor earthquake slip vectors and campaign GPS stations to help define the relative motion direction between the fore-arc block and adjacent plates.

Strain accumulation in adjacent blocks due to locking on block boundaries is calculated by adopting elastic Green's functions and integrating over small patches between the nodes. Surface velocities are predicted using Okada's method (13), applying a slip deficit rate on each small patch defined by adjacent nodes. To quantify inter-SSE locking along the plate interface, a locking

factor ϕ is estimated for each node, defined as the ratio of locked to total slip on the fault, ranging from 0 (freely slipping) to 1 (fully locked), and then smoothed. The inversion scheme uses a grid search and simulated annealing (14) to seek the set of parameters that minimizes data misfit, defined by the reduced χ^2 statistic. To reduce the number of estimated parameters when inverting for the inter-SSE locking pattern, rake is determined by the relative plate or block motion direction.

For SSEs, two approaches were compared: Slip direction is opposite to the direction of plate motion, and slip direction is estimated as a free parameter. In both cases, slip direction (rake) is assumed uniform over the entire plate interface in both space and time; that is, rake variation between patches is not allowed. Results for the two approaches are similar; here we present the case where rake is estimated.

Different along-strike and down-dip parameterization methods for inter-SSE locking and slow slip can also be used to reduce the number of adjustable parameters. In this study, we use the free nodes ("smoothed grid" method) (10) for both inter-SSE locking and SSE displacement to obtain unbiased estimates of patch shape, smoothing results to better represent the inherent spatial resolution of the network, ~30 km (*Spatial Resolution of the Inversions*). We tested the stability of results by performing a large number of inversions under various data weighting and smoothing conditions. Note that results for the 2007.4 SSE are very similar to those presented in ref. 7 even though the data analysis and inversion procedures differ substantially between the two studies. This event is more poorly constrained than later events (*Spatial Resolution of the Inversions*).

Spatial Resolution of the Inversions

Although the node spacing (~10 km beneath the peninsula, somewhat larger offshore) of our mesh can yield slip patch estimates with the same dimensions, this exceeds the inherent spatial resolution of our network, which has a typical station spacing of ~20–30 km. Some form of regularization of the inversion is therefore required. Inversion results (for both inter-SSE locking and SSEs) are therefore smoothed to better reflect network resolution. An initial series of inversions is run to define the tradeoff between smoothing and data misfit; smoothed solutions with data misfit comparable to the known data noise (1) are deemed acceptable (Fig. S1).

We checked the spatial resolving power of the network for inter-SSE locking by conducting a series of "checkerboard" tests, similar to that described in ref. 9. Adjacent patches are assigned to be either fully locked or fully slipping, the corresponding surface displacement is calculated at the existing station locations, random noise is added, and the synthetic dataset is inverted, in this case without smoothing to better illustrate whether individual patches are well-resolved. The test is repeated for various patch sizes, starting with a small patch size (~10 km) and then in multiples of this patch size (~20 km, 30 km, and 40 km). It can be seen in Fig. S2 that patch sizes of 10 and 20 km (*Top*) are not well-resolved. The 30-km patch sizes (third panel) are well-resolved beneath the peninsula, but are less well-resolved offshore. The 40-km patches (*Bottom*) are resolved offshore out to a distance of ~30 km and are less well-resolved beyond this distance.

The resolution of SSE slip patches is similar to the inter-SSE locking, unless individual stations are offline during an event. Fig. S3 shows where the spatial resolution of SSEs is strong (90% or more of the simulated slip is recovered) and moderate (60% or

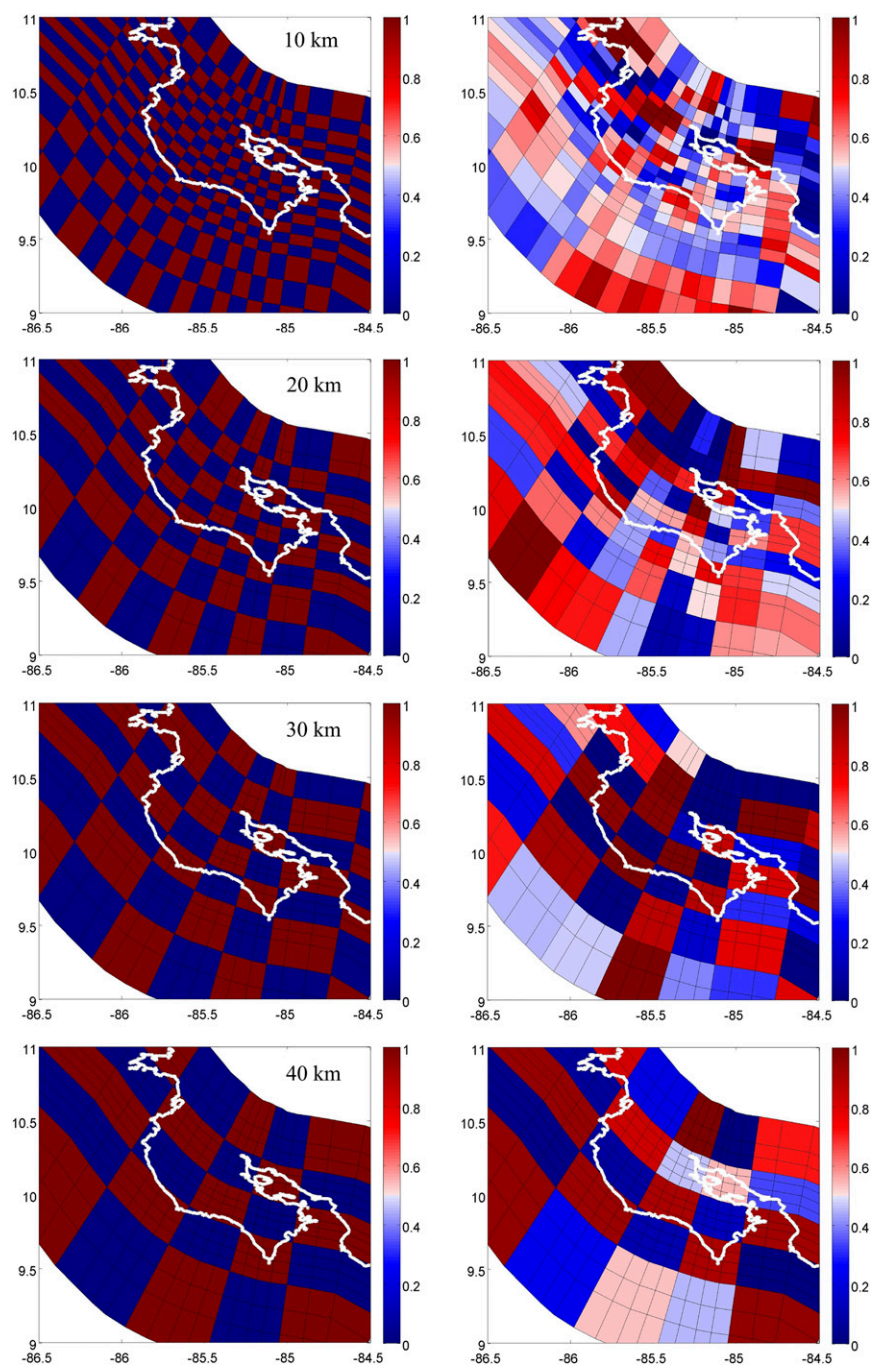
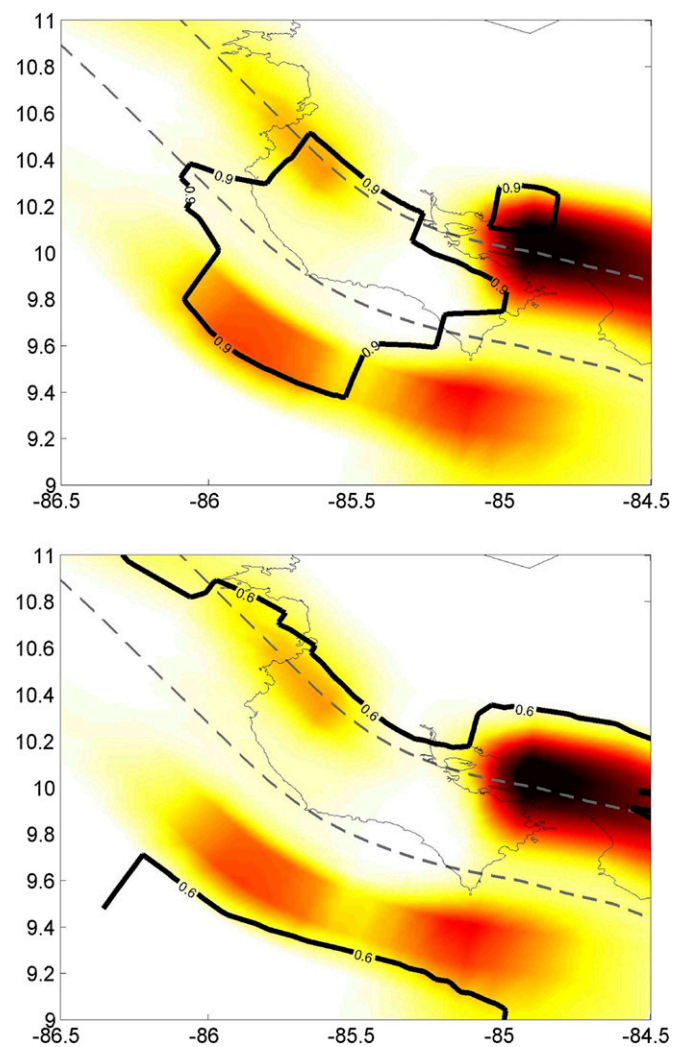


Fig. S2. Checkerboard test of network and inversion resolution. Four different patch sizes are used to determine the minimum resolvable patch size for inter-SSE locking or slow slip (*Left*, input; *Right*, output). The 30-km patches (third panel from top) are resolvable beneath the peninsula. Immediately offshore, 30-km patches are resolvable in some areas, degrading to ~40 km farther offshore (*Bottom*).



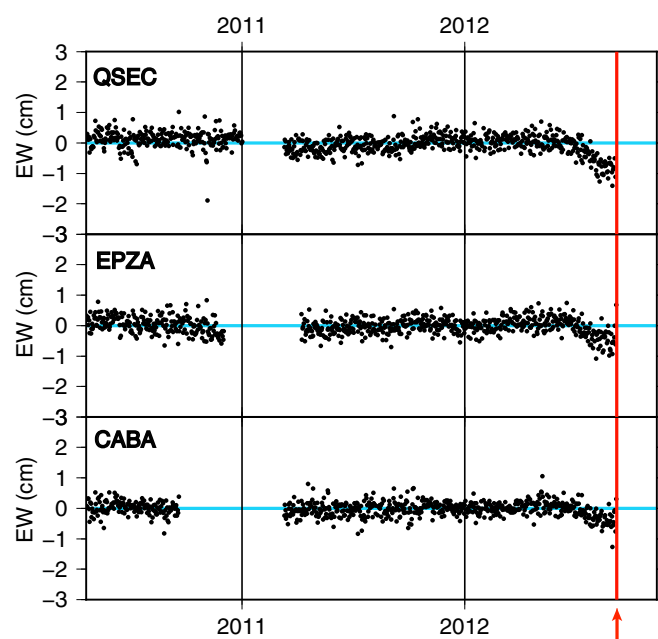


Fig. S4. Detrended displacement time series for the east-west component of three high-precision GPS stations in the Nicoya Peninsula, Costa Rica for 2 y before the 5 September 2012 earthquake (red line and arrow). An SSE beginning several months before the earthquake is evident in all three stations, continuing up to the day of the earthquake.

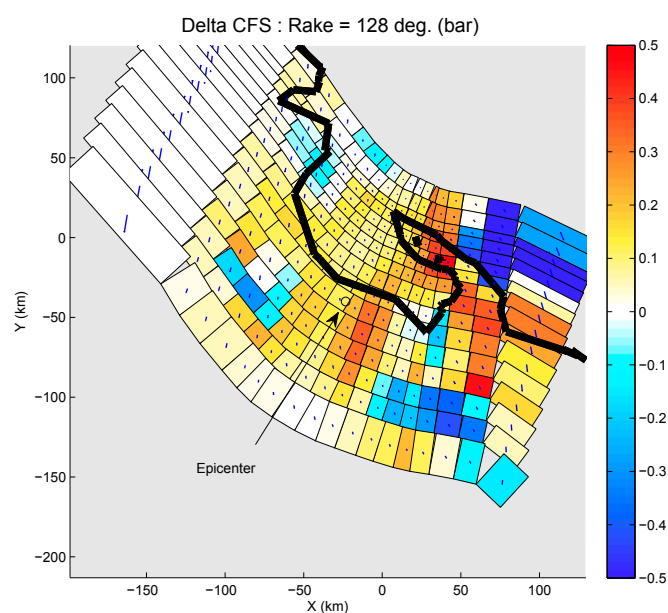


Fig. S5. ΔCFS associated with the 2012 SSE. Red colors indicate changes promoting earthquake rupture, and blue colors indicate changes inhibiting earthquake rupture. Circle and arrow mark the location of rupture initiation of the 2012 earthquake (1).

1. Yue H, et al. (2013) The 5 September 2012 Costa Rica M_w 7.6 earthquake rupture process from joint inversion of high-rate GPS, strong-motion, and teleseismic P wave data and its relationship to adjacent plate boundary interface properties. *J Geophys Res* 118:5453–5466.

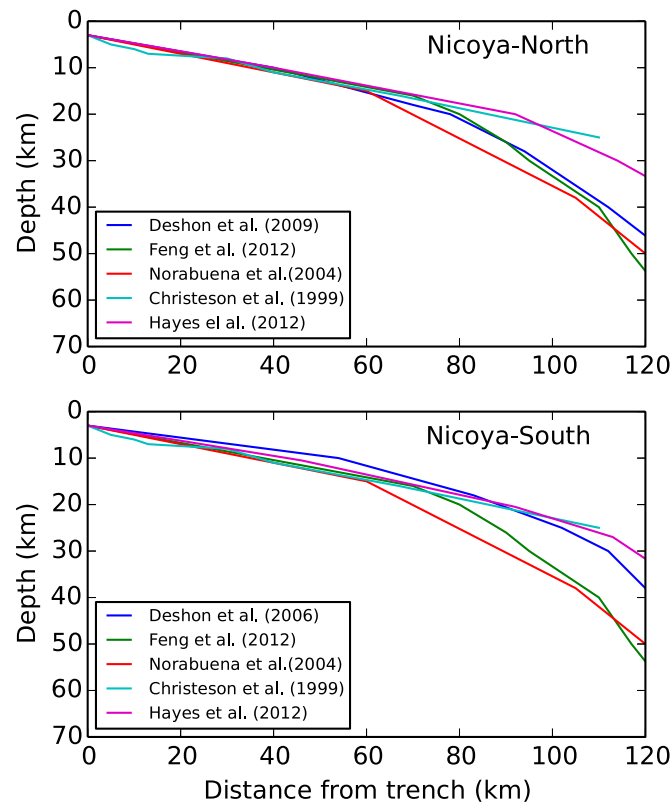


Fig. S6. Comparison of different models for slab geometries beneath the Nicoya Peninsula. Cross-sections are perpendicular to the local trend of the trench. Model references include the following: DeShon et al. (2006) (1), Feng et al. (2013) (2), Norabuena et al. (2004) (3), Christeson et al. (1999) (4), and Hayes et al. (2012) (5).

1. DeShon HR, et al. (2006) Seismogenic zone structure beneath the Nicoya Peninsula, Costa Rica, from three-dimensional local earthquake P- and S-wave tomography. *Geophys J Int* 164: 109–124.
2. Feng L, et al. (2012) Active deformation near the Nicoya Peninsula, northwestern Costa Rica, between 1996 and 2010: Interseismic megathrust coupling. *J Geophys Res* 117, 10.1029/2012JB009230.
3. Norabuena E, et al. (2004) Geodetic and seismic constraints on some seismogenic zone processes in Costa Rica. *J Geophys Res* 109:B11403.
4. Christeson GL, McIntosh KD, Shipley TH, Flueh ER, Goedde H (1999) Structure of the Costa Rica convergent margin, offshore Nicoya Peninsula. *J Geophys Res* 104:25,443–25,468.
5. Hayes GP, Wald DJ, Johnson RL (2012) Slab1.0: A three-dimensional model of global subduction zone geometries. *J Geophys Res* 117:B01302.